

3D printed dielectric rectangular waveguides, splitters and couplers for 120 GHz

M. WEIDENBACH,¹ D. JAHN,¹ A. REHN,¹ S. F. BUSCH,¹ F. BELTRÁN-MEJÍA,² J. C. BALZER,^{1,*} AND M. KOCH¹

¹Department of Physics and Materials Sciences Center, Philipps-Universität Marburg, Renthof 5, 35032 Marburg, Germany

²National Institute of Telecommunications-Inatel, Av. João Camargo 510, 37540-000 Santa Rita do Sapucaí /MG, Brazil

*jan.balzer@physik.uni-marburg.de

Abstract: We use a 3D printer to fabricate rectangular dielectric single mode waveguides for 120 GHz. The rectangular waveguides consisting of polystyrene showed an attenuation of 6.3 dB/m, which is low enough for short devices. We also characterize 3D printed Y-splitters and a 1x3-splitter based on multimode interference. Further, we construct and measure a variable planar waveguide coupler which can be used as a 3-dB coupler, a cross-coupler and no coupler at all.

© 2016 Optical Society of America

OCIS codes: (130.5460) Polymer waveguides; (350.4010) Microwaves; (230.1360) Beam splitters.

References and Links

1. P. U. Jepsen, D. G. Cooke, and M. Koch, "Terahertz spectroscopy and imaging - Modern techniques and applications," *Laser Photonics Rev.* **5**(1), 124–166 (2011).
2. M. Tonouchi, "Cutting-edge terahertz technology," *Nat. Photonics* **1**(2), 97–105 (2007).
3. A. Soltani, S. F. Busch, P. Plew, J. C. Balzer, and M. Koch, "THz ATR spectroscopy for inline monitoring of highly absorbing liquids," *J. Infrared Millim. Terahertz Waves* **37**(10), 1001–1006 (2016).
4. R. Gente, S. F. Busch, E. M. Stübling, L. M. Schneider, C. B. Hirschmann, J. C. Balzer, and M. Koch, "Quality Control of Sugar Beet Seeds With THz Time-Domain Spectroscopy," *IEEE Trans. Terahertz Sci. Technol.* **6**, 754–756 (2016).
5. R. A. Kaundl, D. Hägele, M. A. Carnahan, and D. S. Chemla, "Transient terahertz spectroscopy of excitons and unbound carriers in quasi-two-dimensional electron-hole gases," *Phys. Rev. B* **79**(4), 45320 (2009).
6. D. M. Mittleman, J. Cunningham, M. C. Nuss, and M. Geva, "Noncontact semiconductor wafer characterization with the terahertz Hall effect," *Appl. Phys. Lett.* **71**(1), 16 (1997).
7. E. R. Brown, J. E. Bjarnason, A. M. Fedor, and T. M. Korter, "On the strong and narrow absorption signature in lactose at 0.53 THz," *Appl. Phys. Lett.* **90**(6), 61908 (2007).
8. M. Walther, P. Plochocka, B. Fischer, H. Helm, and P. Uhd Jepsen, "Collective vibrational modes in biological molecules investigated by terahertz time-domain spectroscopy," *Biopolymers* **67**(4-5), 310–313 (2002).
9. T. Kleine-Ostmann, R. Wilk, F. Rutz, M. Koch, H. Niemann, B. Güttler, K. Brandhorst, and J. Grunenberg, "Probing noncovalent interactions in biomolecular crystals with terahertz spectroscopy," *ChemPhysChem* **9**(4), 544–547 (2008).
10. T. Kleine-Ostmann and T. Nagatsuma, "A review on terahertz communications research," *J. Infrared Millim. Terahertz Waves* **32**(2), 143–171 (2011).
11. R. Piesiewicz, M. Jacob, M. Koch, J. Schoebel, and T. Kurner, "Performance analysis of future multigigabit wireless communication systems at THz frequencies with highly directive antennas in realistic indoor environments," *IEEE J. Sel. Top. Quantum Electron.* **14**(2), 421–430 (2008).
12. B. Scherger, M. Scheller, C. Jansen, M. Koch, and K. Wiesauer, "Terahertz lenses made by compression molding of micropowders," *Appl. Opt.* **50**(15), 2256–2262 (2011).
13. B. Scherger, C. Jördens, and M. Koch, "Variable-focus terahertz lens," *Opt. Express* **19**(5), 4528–4535 (2011).
14. A. D. Squires, E. Constable, and R. A. Lewis, "3D printed terahertz diffraction gratings and lenses," *J. Infrared Millim. Terahertz Waves* **36**(1), 72–80 (2015).
15. B. Scherger, N. Born, C. Jansen, S. Schumann, M. Koch, and K. Wiesauer, "Compression molded terahertz transmission blaze-grating," *IEEE Trans. Terahertz Sci. Technol.* **2**(5), 556–561 (2012).
16. J. Liu, R. Mendis, and D. M. Mittleman, "The transition from a TEM-like mode to a plasmonic mode in parallel-plate waveguides," *Appl. Phys. Lett.* **98**, 128–130 (2011).
17. K. Nielsen, H. K. Rasmussen, P. U. Jepsen, and O. Bang, "Porous-core honeycomb bandgap THz fiber," *Opt. Lett.* **36**(5), 666–668 (2011).

18. S. Atakaramians, S. Afshar V, T. M. Monro, and D. Abbott, "Terahertz dielectric waveguides," *Adv. Opt. Photonics* **5**(2), 169 (2013).
19. C. Jördens, K. L. Chee, I. A. I. Al-Naib, I. Pupeza, S. Peik, G. Wenke, and M. Koch, "Dielectric fibres for low-loss transmission of millimetre waves and its application in couplers and splitters," *J. Infrared Millim. Terahertz Waves* **31**, 214–220 (2010).
20. E. G. Geterud, P. Bergmark, and J. Yang, "Lightweight waveguide and antenna components using plating on plastics," in *2013 7th European Conference on Antennas and Propagation (EuCAP)* (2013), pp. 1812–1815.
21. J. Liu, R. Mendis, and D. M. Mittleman, "A Maxwell's fish eye lens for the terahertz region," *Appl. Phys. Lett.* **103**(3), 031104 (2013).
22. S. Pandey, B. Gupta, and A. Nahata, "Terahertz plasmonic waveguides created via 3D printing," *Opt. Express* **21**(21), 24422–24430 (2013).
23. A. Bisognin, D. Titz, F. Ferrero, R. Pilard, C. A. Fernandes, J. R. Costa, C. Corre, P. Calascibetta, J.-M. Riviere, A. Poulain, C. Badard, F. Giansello, C. Luxey, P. Busson, D. Gloria, and D. Belot, "3D printed plastic 60 GHz lens: Enabling innovative millimeter wave antenna solution and system," in *2014 IEEE MTT-S International Microwave Symposium (IMS2014)* (IEEE, 2014), pp. 1–4.
24. W. D. Furlan, V. Ferraro, J. A. Monsoriu, P. Zagrajek, E. Czerwińska, and M. Szustakowski, "3D printed diffractive terahertz lenses," *Opt. Lett.* **41**(8), 1748–1751 (2016).
25. N. Yudasari, J. Anthony, and R. Leonhardt, "Terahertz pulse propagation in 3D-printed waveguide with metal wires component," *Opt. Express* **22**(21), 26042–26054 (2014).
26. A. L. S. Cruzl, V. Serrao, C. L. Barbosa, M. A. R. Franco, C. M. B. Cordeiro, A. A. Argyros, and X. Tang, "3D printed hollow core fiber with negative curvature for terahertz applications," *J. Microwaves. Optoelectron. Electromagn. Appl.* **14**, 45–53 (2015).
27. S. F. Busch, M. Weidenbach, M. Fey, F. Schäfer, T. Probst, and M. Koch, "Optical properties of 3D printable plastics in the THz regime and their application for 3D printed THz optics," *J. Infrared Millim. Terahertz Waves* **35**(12), 993–997 (2014).
28. S. F. Busch, M. Weidenbach, J. C. Balzer, and M. Koch, "THz Optics 3D Printed with TOPAS," *J. Infrared Millim. Terahertz Waves* **37**(4), 303–307 (2016).
29. R. G. Hunsperger, *Integrated Optics: Theory and Technology*, 6th ed. (Springer, 2009).
30. A. F. Oskooi, D. Roundy, M. Ibanescu, P. Bermel, J. D. Joannopoulos, and S. G. Johnson, "MEEP: A flexible free-software package for electromagnetic simulations by the FDTD method," *Comput. Phys. Commun.* **181**(3), 687–702 (2010).
31. W. A. Gambling, H. Matsumura, and C. M. Ragdale, "Curvature and microbending losses in single-mode optical fibres," *Opt. Quantum Electron.* **11**(1), 43–59 (1979).
32. L. B. Soldano, *Multimode Interference Couplers Design and Applications* (Delft University, 1994).
33. S. L. Chuang, *Physics of Optoelectronic Devices* (Wiley, 1995).
34. M. Reuter, N. Vieweg, B. M. Fischer, M. Mikulicz, M. Koch, K. Garbat, and R. Dąbrowski, "Highly birefringent, low-loss liquid crystals for terahertz applications," *APL Mater.* **1**(1), 012107 (2013).

1. Introduction

Over the last 20 years, there have been tremendous efforts to bridge the so-called "THz gap", spanning frequencies from 0.1 THz to 10 THz where technology is not yet as well developed as in the optical and microwave wavelengths [1]. Electronic sources and detectors approach the gap from the low-frequency part of the electromagnetic spectrum, while optoelectronic conversion techniques are applied to gain access from the high-frequency part [2]. The interest to develop the THz range is manifold: Since many commonly used materials like wood and plastic are transparent for THz radiation, it is a well-suited tool for nondestructive testing [3,4]. It developed also to an important tool for basic research, due to its high sensitivity to free electrons [5,6]. Further, many molecules and crystal lattices show a spectral fingerprint in the THz frequency range [7–9]. However, from an economical point of view, telecommunication engineering can become one of the most important future application of THz technology [10,11]. The ever-growing demand for higher data transmission rates can only be satisfied by developing new telecommunication frequencies. Therefore, not only new sources and detectors have to be investigated, but also passive devices like lenses [12,13], gratings [14,15], waveguides [16–18] and splitters [19].

Dielectric waveguides for visible and infrared light are well understood and are used in commercial applications. There have also been efforts to investigate waveguides in the THz frequency range [18]. The traditional methods for dielectric waveguide fabrication are lithographic structuring of silicon—mainly for devices operating in the visible/infrared—and CNC milling of transparent polymers like HDPE for microwave devices. However, these

methods are time-consuming, expensive and need a sophisticated infrastructure. Here we study the performance of 3D printed dielectric waveguides. 3D printing as a rapid prototyping technique is suitable especially in the THz frequency range where the requirements on the surface quality are low due to the long wavelength (1 THz equates to 300 μm) of the radiation. Recently, 3D printing technology has been used to fabricate waveguides and lenses for the GHz and THz frequency range [20–22]. However, these devices had to be coated with metal to achieve a conducting surface. Examples of 3D printed dielectric devices are printed lenses for 60 GHz [23], gratings and lenses for the THz frequency range [14,24] and hollow core THz waveguides [25,26].

In this paper we want to concentrate on the investigation of dielectric waveguides for 120 GHz. In the following sections, we characterize propagation and bending losses of the proposed waveguides. As sample devices, we fabricate and analyze a Y-shaped 1x2 beam splitter, a 1x3 multimode interference splitter and a planar waveguide coupler. Finally we introduce our final remarks to discuss about the results and future perspectives.

2. Design, Fabrication and Experimental Setup

A material suitable for waveguides must have a low absorption as well as a low dispersion for the used frequencies. Since we want to use a 3D printer to fabricate the waveguides, a third requirement has to be fulfilled: The material has to be well printable. Important parameters here are, for example, the glass transition temperature and the thermal expansion coefficient. Previously, it has been shown that polystyrene (PS) meets these requirements. The absorption at 500 GHz is 0.42 cm^{-1} while the refractive index between 0.5 and 3 THz is flat and has a value of 1.56 [27]. On the other hand, using TOPAS would be a better option, since this material has an even lower absorption [28]. However, the 3D printing filaments are not commercially available.

For the waveguide fabrication, we use an Ultimaker Original 3D printer which is upgraded with a customized heating bed. It can be heated up to 60°C. All devices are printed with a 400 μm nozzle at a temperature of 235°C on a glass plate. The layer height (layer resolution) and printing speed are chosen to be 100 μm and 25 mm/s respectively. The typically achievable line width (lateral resolution) is around 400 μm , which is connected to the nozzle size. We use a plastic protective lacquer for circuit boards to achieve a good adhesion between the glass plate and the printed material.

For the waveguides, it is desirable to design the cross-section for single mode operation and a good mode confinement. This leads to a trade-off, since the confinement of the fundamental mode improves with increasing cross section, whereas the cutoff frequency of higher modes decreases. If a certain cross-section is exceeded and the cutoff frequency undercuts 120 GHz, the waveguide can maintain more than the fundamental EH_{11} mode. In order to find the optimal waveguide dimensions, COMSOL Multiphysics® is used to calculate the mode distribution of different cross-sections numerically. A parameter sweep of the height and the width of the waveguide revealed that 1.5 mm x 1.5 mm is still single-mode while confinement losses are still negligible. For slightly bigger cross-sections multimode operation occurred, hence all waveguides are fabricated with a 1.5 mm x 1.5 mm cross-section. For this squared waveguide fabricated out of polystyrene, the computed effective refractive index for the fundamental mode at 120 GHz was $n_{\text{eff}} = 1.287$.

To ensure that only radiation guided by the waveguide is detected, every waveguide is fabricated with a 90° bend. Also, thin PS supports with a height of 0.2 mm are included via 3D printing in order to mount the waveguides. These supports are thin enough to have a negligible effect on the waveguide. With these, different waveguide devices are fabricated as Fig. 1 depicts a schematic overview of the 3D printed geometries. These include (a–c) waveguides with different radii and different lengths for the evaluation of bending losses and propagation losses and more complex devices like (d, e) splitters, (f) a multimode-

interference (MMI) 1x3 splitter and (g) a variable directional coupler. A detailed explanation of these devices is given below.

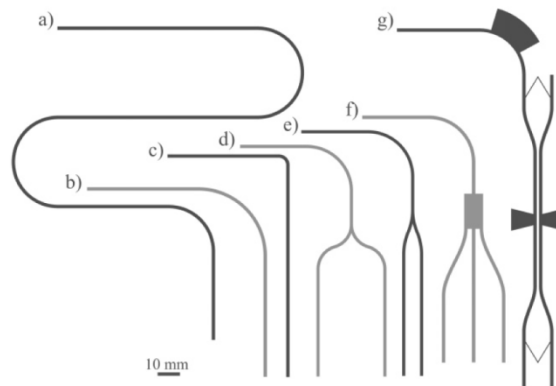


Fig. 1. Schematic overview over the printed waveguides. a) S-shaped waveguide with a length of 506 mm for propagation loss measurement (due to the limited size of the 3D printer more bends were necessary to achieve the desired length), b) bending radius $r = 30$ mm and c) $r = 4$ mm for the measurement of bending losses with a length of 151 mm, d) and e) Y splitters with arm distances $dx = 30$ mm and $dx = 8$ mm, f) MMI 1x3 splitter, g) variable waveguide coupler. This is not an exhaustive list of the waveguides used in the experiments.

For the experimental setup, a 120 GHz CW microwave system from QuinStar Technology (QTM-C015RF, QEA-C0FBFP) is used. The transceiver's Gunn diode provides vertical linear polarized radiation with an output power of 30 mW. The receiver is mounted on a motorized XYZ-stage which allows easy adjustment of the setup and spatially resolved measurements of the electrical field behind the devices under test (e.g. the waveguides). Both antennas have a horn antenna attached, in which the dielectric waveguides were placed (see Fig. 2). With this approach (end-butt coupling) a very efficient coupling can be achieved since the size of the waveguide is similar to the source's size. However, the coupling efficiency oscillated strongly in dependence of the spacing between waveguide and source which complicates a proper adjustment. These oscillations are caused by Fabry-Pérot resonances formed between the faces of the waveguide and emitter [29]. For this reason, and to ensure comparability between the data of the different waveguides, we carefully align the setup for the highest achievable signal for each waveguide. For the spatially resolved measurements of the electric field, the horn antenna of the receiver is detached. In this way, only the small detection area of the receiver is used to sample the electric field which increases the spatial resolution of the measurements.

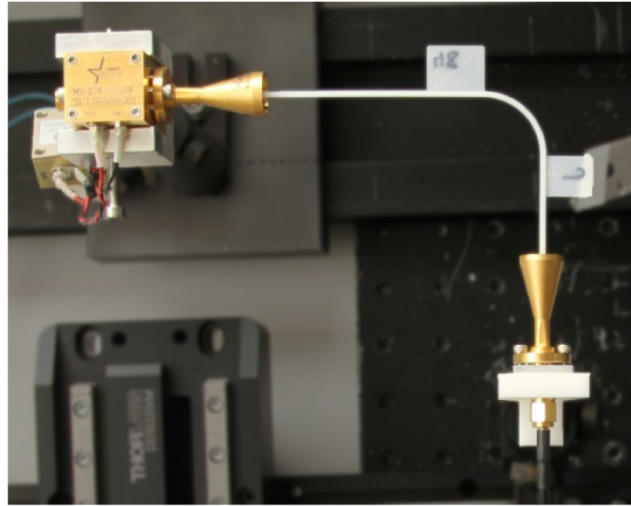


Fig. 2. Top view of the experimental setup. Transceiver (upper left) and receiver have both attached a horn antenna. A waveguide is placed inside the horns (end-butt coupling) and mounted on a blade using one of the thin supports.

3. Characterization

In order to better understand the performance of these waveguides, basic properties like bending and absorption losses are investigated. First, we measure bending losses for different curvature radius. With these results we are able to include 90° bends in all of our structures to eliminate unguided radiation at the receiver with negligible bending losses. Then we examine the propagation losses of the printed waveguides, as they are important to predict the general usability of our 3D printed devices.

At first, the bending losses are examined by measuring the dependence of the radius on the transmission through waveguides with a constant length of 151 mm. Figure 3(a) shows the transmitted intensity through bends of 90° for radii between 0.7 mm and 40.7 mm. The intrinsic attenuation of the waveguides is eliminated by normalizing all values to the maximum value, which is measured at the largest radius of 40.7 mm. For $r < 10$ mm the radiation leaks noticeably out of the waveguide with strongly increasing loss for smaller radii. The dotted line in Fig. 3(a) represents losses in a waveguide bend by using the theoretical approach presented by Hunsperger [29]. Besides, numerical results for simulations are depicted with the dashed line. These numerical results are obtained by using a Finite-Difference Time-Domain method open-source software (MEEP [30]). Experimental results are depicted with the solid line and it can be seen there is a good resemblance with the theoretical and numerical results. On the inset of Fig. 3(a), a similar trend can be observed for the exponential behavior of the extinction. The deviation for small radii as depicted in the inset of Fig. 3(a) has several origins: First, the theory does not apply for radii which are small compared to the width of the waveguide. Second, for $r < 3$ mm higher order modes are excited in the waveguide—as additional experiments have demonstrated—and such modes are not included in the theory of Hunsperger. Based on these results, from here on we used $r = 20$ mm for all 90° bends and $r > 10$ mm for splitters; since this way we can obtain low bending losses combined with a compact footprint. Indeed, this is advantageous for the 3D printing process and reduces the propagation losses since the additional path length due to the bend is kept low.

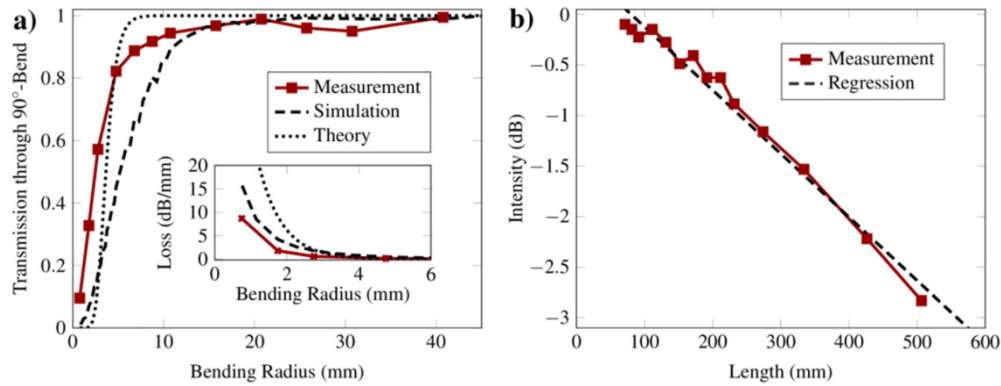


Fig. 3. a) Transmission through a 90° bend in dependence of its bending radius and (inset) resultant loss per length for small radii. Experimental measurements (solid line), numerical simulations (dashed line) and theoretical calculation (dotted line) show similar behavior with deviations for small radii. b) Output intensity after propagating through waveguides of different length including a 90° bend with a 20 mm curvature radius (solid line). The attenuation could be calculated with the slope of a linear fit (dashed line) to be 6.3 dB/m.

As the next step, we examine the propagation losses of the waveguides by measuring the transmitted intensity through waveguides of different lengths. The solid line in Fig. 3(b) shows the attenuation on a logarithmic scale. The behavior of the transmitted intensity P_1 can be described by the Beer-Lambert law: $P_1(I) = P_0 \cdot e^{-\alpha \cdot l}$, where the initial intensity P_0 decreases exponentially with increasing length l . The absorption coefficient α can be calculated by the slope of a linear fit in Fig. 3(b), as shown by the dashed line to be $\alpha = 1.45 \pm 0.13 \text{ m}^{-1}$ which equals an attenuation of $6.3 \pm 0.6 \text{ dB/m}$. Up to now, the total length of 3D printed devices is not likely to exceed 0.5 m due to limited dimensions of 3D printers, therefore the attenuation can be neglected in this case.

After knowing the bending and absorption losses for our basic waveguide, we fabricated Y-splitters which are supposed to split the power equally into two arms. The schematic for the waveguide based splitters is depicted in Fig. 4(a). The splitter consists of circle segments, the radii of which depend on the desired distance between the two arms dx and the vertical distance dz . Several splitters with distances of $dx = 4 \dots 30 \text{ mm}$ and $dz = 20 \text{ mm}$ are printed, ensuring that the minimal radius was greater than 10 mm to keep bending losses low. Raster scanned output images of the splitters with $dx = 8 \text{ mm}$ and 30 mm in Figs. 4(b) and 4(c) show that even for the very intense split of $dx = 30 \text{ mm}$ almost no radiation leaves the waveguide.

Moreover, the splitters are analyzed regarding their imbalance ($I = 10 \cdot \log(P_{\max} / P_{\min})$) and the sum of the output power ($P_1 + P_2$). More precisely, for a perfect splitter with balanced coupling and with no losses, I shall be equal zero and the sum of the output powers shall be as high as the input power P_0 . Although the radiation losses are not very high even for big distances, small splits have lower loss and smaller imbalance as shown in Fig. 4(d). The increasing loss for larger separations is caused by smaller radii and therefore the increasing abrupt transition between the curvature radii of the curved sections of the waveguide [31]. The imbalance might originate from bouncing waves induced by the 90° bend. To evaluate this, the 15 mm long part between curve and split of the splitter with $dx = 20 \text{ mm}$ is continuously narrowed with a knife to a width of 1.3 mm. An additional measurement shows that the imbalance is now reduced even below 0.1 dB, which gives evidence of bouncing waves.

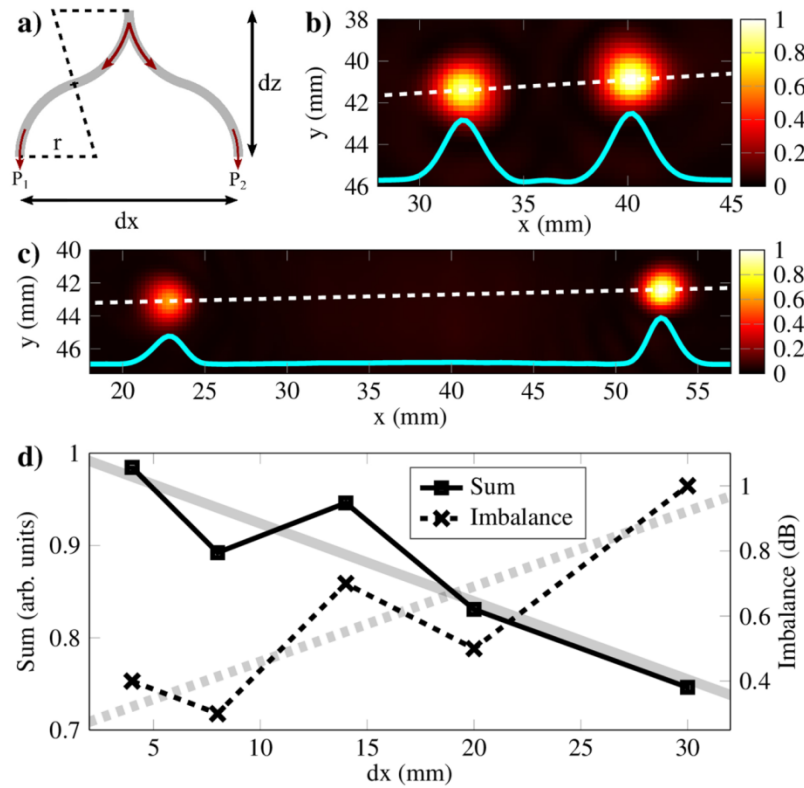


Fig. 4. a) Schematic of a 1x2 splitter. b), c) Output images of these splitters with split intensity of $dx = 8$ mm and 30 mm. In the image of the wide split a slight loss through the splitter's middle is visible. The cyan curve depicts the intensity measured along the white dashed line. d) Sum and imbalance of the output power of the two channels for different dx . The grey lines are linear regressions which show the trend of the measurements for the sum of the power (solid) and the imbalance (dashed).

As a demonstration of a more complex splitter, we fabricate a multimode interference (MMI) splitter as shown in Fig. 1(f). Here we take advantage of the self-imaging principle [32] where a multimode waveguide exhibits some maxima along the x-axis as in [19]. In this work, we present a 1x3 splitter. However, more output channels can also be achieved by changing the dimensions of the multimode section of the MMI splitter. The required dimensions are calculated by using an analytical approach [32] with a subsequent numerical optimization. The optimal dimension of the multimode section is found to be 8.5 mm x 15.75 mm.

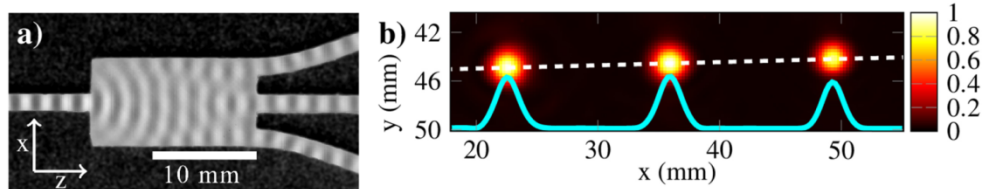


Fig. 5. a) Picture of the MMI 1x3 splitter with the simulated electric field E_y overlaid. The radiation interferes with itself causing three maxima at the end of the rectangle, where output waveguides are attached. b) A raster scanned image of the intensity measured at the output. Power was distributed with good balance and no radiation between the output waveguides was observed. The cyan curve depicts the intensity measured along the white dashed line.

Figure 5(a) shows a picture of the 1x3 splitter's MMI section with the simulated electric field overlaid. It can be seen that the different radiation paths interfere constructing three maxima at the end of the rectangular multimode section where the output waveguides are attached. In Fig. 5(b), the spatially resolved intensity of the output fibers for the 1x3 splitter is depicted. The intensity distribution shows an imbalance of 0.9 dB.

Finally, we design and fabricate a variable waveguide coupler, which can be switched continuously. This device can work as a cross-coupler, a power divider or no coupler at all. It consists of two 60 mm long parallel waveguides (main and coupled line) linked by thin connections which act as springs and allow to change the distance d between both arms. A picture of the fabricated device can be seen in Fig. 6(b). If both arms are close enough to each other, super-modes occur, leading to mode beating between main and coupled line.

These super-modes act as coupled oscillators with even (evenly oscillating fields in both arms) and odd (contrary oscillating fields) modes with different propagation constants β_{even} and β_{odd} . As a consequence, the power couples between the lines while propagating through the waveguide. The length after which the whole power has coupled from one to the other line is called beat length (L_b) and it depends on the difference of the propagation constants of the even and the odd mode of the system [33]: $L_b = \pi / (\beta_{\text{even}} - \beta_{\text{odd}})$. For this reason, the propagation constants β_{even} and β_{odd} were computed numerically for several distances between the waveguides. It turned out that $L_b(d)$ can be described by an exponential function. In theory, the power at the output ports P_2 and P_3 follows the equations $P_2 = P_1 \cdot \cos^2(C \cdot z)$ and $P_3 = P_1 \cdot \sin^2(C \cdot z)$, where $C = \pi / (2L_b)$ and $z = 60$ mm is the coupling length as can be seen in Fig. 6(a). From these equations follows that the output powers in both ports oscillate with exponentially decreasing frequency.

In the experiment, the coupling distance between the waveguides is varied from 0 to 3 mm by moving the supports attached at each line with a linear stage. An image of the output plane is recorded for every step by moving the detector antenna. Due to the sensitivity of the waveguide coupler regarding the distance between the waveguides, contactless measurements become necessary. For both spots in the image, the maximum intensity is extracted from the raster scanned images and plotted in Fig. 6(b). With increasing distance, the power oscillates from P_2 (black line) to P_3 (red line) with exponentially decreasing frequency, as predicted by the theory (dashed lines). For big distances, the beat length exceeds the coupling length by far so that the coupled power goes to zero. Also, at a distance of 0.86 mm the beat length is equal to the length of the lines ($L_b = z$) and the whole power is transferred from the main line to the coupled line. In addition, at 0.4 mm the beat length is short enough so that the power couples back to the main line before leaving the coupler ($L_b = z/2$). As expected, the minimum beat length $z/4$ is reached when both lines were placed next to each other. In comparison to the calculation, the measured results are shifted towards larger distances. This might originate from a distortion of the main and coupled line, which are not always parallel, even more for big distances. As a result, the effective mean distance is smaller than denoted. Also, the effective coupling length is slightly greater than 60 mm due to coupling effects in the converging parts of the two lines.

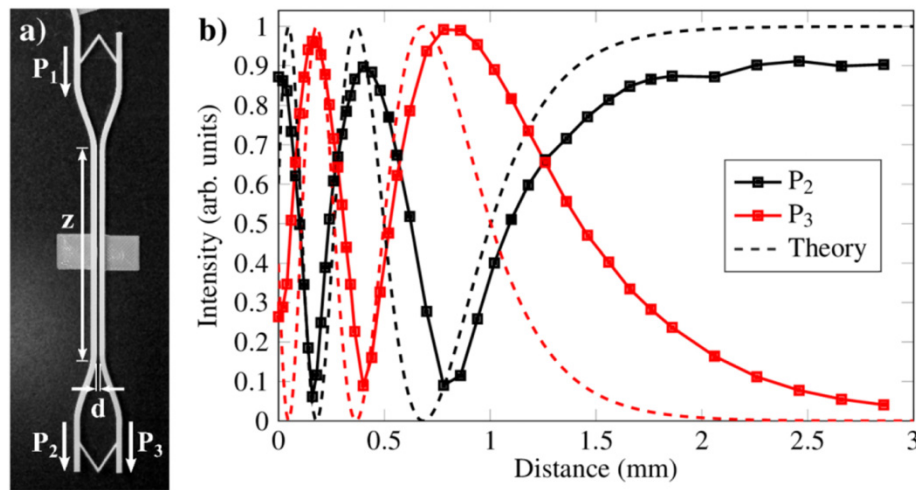


Fig. 6. a) Picture of the variable directional coupler. b) The intensity distribution at the output ports as a function of the distance between main (P_2) and coupled line (P_3). The frequency of the oscillation decreases with increasing distance. Dashed lines represent theoretical calculations for a waveguide directional coupler as in [33].

4. Conclusion and Outlook

In summary, we have designed and fabricated 3D printed dielectric rectangular waveguides for 120 GHz made out of polystyrene. The cross section was 1.5 mm x 1.5 mm which allowed single mode operation with low confinement losses. These waveguides had an intrinsic attenuation of 6.3 dB/m and a critical bending radius of slightly below 10 mm. For bigger radii, the bending losses can be neglected. We have also fabricated 1x2 splitters and a multimode-interference 1x3 splitter with low losses and imbalances around 0.7 dB.

Also, a planar waveguide coupler with variable coupling properties was demonstrated. By varying the gap between main and coupled line, the power ratio between both arms could be changed and the results are in good agreement with the theory. This variable waveguide coupler worked as intended and was very sensitive to distortions for small distances. It and could be useful for sensing applications or to construct a THz switch.

For future work, we plan to fabricate electrically tunable components, such as Mach-Zehnder interferometers and couplers with integrated liquid crystals [34]. Further, we plan to investigate these printed waveguides with a THz time-domain spectroscopy (TDS) system from 0.1 THz to 3 THz in order to prove the feasibility of these devices for frequencies higher than 120 GHz. We are confident that 3D printing will become a valuable tool for rapid prototyping of even more complex structures for THz frequencies.